Calibration of Upper Air Water Vapour Profiles Using the IPRAL Raman Lidar and ERA5 Model Results and Comparison to GRUAN Radiosonde Observations

Dunya Alraddawi, Philippe Keckhut, Florian Mandija, Alain Sarkissian, Christophe Pietras, Jean-Charles Dupont, Antoine Farah, Alain Hauchecorne, Jacques Porteneuve

atmosphere

MDPI

Article

Calibration of Upper Air Water Vapour Profiles Using the IPRAL Raman Lidar and ERA5 Model Results and Comparison to GRUAN Radiosonde Observations

Dunya Alraddawi [1,*], Philippe Keckhut [1], Florian Mandija [1], Alain Sarkissian [1], Christophe Pietras [2], Jean-Charles Dupont [3], Antoine Farah [4], Alain Hauchecorne [1,5] and Jacques Porteneuve [5]

1 Laboratoire Atmosphères, Observations Spatiales (LATMOS), Institut Pierre-Simon Laplace (IPSL), Université de Versailles-Saint-Quentin-en-Yvelines (UVSQ)/Paris-Saclay University, Sorbonne University, Centre National de la Recherche Scientifique (CNRS), 78280 Guyancourt, France; philippe.keckhut@latmos.ipsl.fr (P.K.); florian.mandija@latmos.ipsl.fr (F.M.); alain.sarkissian@latmos.ipsl.fr (A.S.); alain.hauchecorne@latmos.ipsl.fr (A.H.)
2 Laboratoire de Météorologie Dynamique, École Polytechnique, CNRS, 91128 Palaiseau, France; christophe.pietras@lmd.ipsl.fr
3 Institut Pierre-Simon Laplace, École Polytechnique, UVSQ, Université Paris-Saclay, 92331 Palaiseau, France; jean-charles.dupont@ipsl.fr
4 MeteoModem, 77300 Fontainebleau, France; afarah@meteomodem.com
5 Gordien Strato, 91370 Verrière le Buisson, France; jacques.porteneuve@latmos.ipsl.fr
* Correspondence: dunya.alraddawi@latmos.ipsl.fr

Abstract: Accurate measurements of upper troposphere humidity are essential to enhance understanding of contrail formation and guiding mitigation efforts. This study evaluates the ability of the IPRAL Raman Lidar, located south of Paris, to provide high-resolution water vapour mixing ratio (WVMR) profiles at contrail-relevant altitudes. Raman signals are screened on hourly bases, and a universal calibration method, independent of acquisition mode, is proposed towards operational Lidar water vapour profiles, using co-located ERA5 data. Calibration factors are derived from comparisons between 4 and 6 km, and nightly coefficients determined from hourly factors. Instrumental stability is monitored through the temporal evolution of calibration factors, and stable-period medians are adopted as final values. The uncertainty of calibrated WVMR profiles is assessed by comparison with GRUAN processed Meteomodem M10 radiosondes and ERA5 data. Results show a high agreement (>90%), with IPRAL exhibiting a small negative bias (~10%) below 8 km, reducing to ~5% up to 10.5 km to radiosondes. ERA5 systematically underestimates water vapour at cruise altitudes, with a dry bias increasing from 10% at 9 km to >20% at 11 km. Recent IAGOS corrections to ERA5, improving supersaturation representation, are validated over Paris. This calibrated Lidar data set supports improved atmospheric modelling and contributes to future air traffic management strategies.

Keywords: Raman Lidar; water vapour profile; calibration; ERA5; radiosondes; upper troposphere

Academic Editor: Xin Ma

Received: 23 January 2025
Revised: 21 February 2025
Accepted: 14 March 2025
Published: 20 March 2025

Citation: Alraddawi, D.; Keckhut, P.; Mandija, F.; Sarkissian, A.; Pietras, C.; Dupont, J.-C.; Farah, A.; Hauchecorne, A.; Porteneuve, J. Calibration of Upper Air Water Vapour Profiles Using the IPRAL Raman Lidar and ERA5 Model Results and Comparison to GRUAN Radiosonde Observations. *Atmosphere* **2025**, *16*, 351. https://doi.org/10.3390/atmos16030351

1. Introduction

Contrails (condensation trails) contribute to the non CO_2 radiative forcing of aviation on climate, which drives recent worldwide mitigation efforts [1–4]. Climate-impacting contrails are possibly formed by aircraft exhaust at typical flight levels when the exhaust fumes encounter the so-called ice-supersaturated regions (ISSR) [5,6]. Thus, their formation and persistence are strongly influenced by ambient relative humidity with respect

to ice (RHi). Towards Better Contrails Mitigation, the European funded project (BeCoM) (https://becom-project.eu/; Accessed on 13 March 2025) aims to optimise aviation trajectories, to avoid aircraft-induced persistent contrails formation. Such objective is limited by the current capacities to model the favourite thermodynamics to contrail occurrence, persistence, and evolution.

The main uncertainty in contrails forecasting is supersaturation humidity levels assimilation, which is complicated by the lack of accurate humidity data, most challenging to measure at cruise altitudes being affected by both large- and small-scale dynamics as well as cloud processes [7–10]. In the BeCoM project, we try to assess the current uncertainties of humidity measurements using commercial aircraft (like In-Service Aircraft for a Global Observing System IAGOS) [11], and in situ instruments to provide crucial upper troposphere observations [10].

Raman Lidar, a laser-based active optical remote sensing technique, albeit limited by low clouds presence, offers a method to characterise mid and high cloud locations and vertical extension at a high vertical/temporal resolution. Space-based Lidar (ex: [12]), airborne-based Lidar (ex: [13]), and ground-based Lidar [14,15] are valuable for studying cirrus clouds and aircraft-induced contrails, where Lidar observations, integrated over short time scales (a few minutes) allow for detailed assessments of supersaturation conditions [16]. However, only ground-based Lidar can offer additional simultaneous ambient water vapour vertically resolved information [17,18].

Raman Lidar water vapour mixing ratio is proportional to the ratio of the H_2O and N_2 Raman wavelengths signals. A calibration process is conducted to give a physical meaning of this ratio, to be converted on a real WVMR by a scale factor. Hence, accurate Raman Lidar water vapour retrievals are subject to the calibration uncertainties.

Raman Lidar WVMR has three commonly used calibration methods: internal calibration, external calibration, and hybrid calibration [19,20] methods. The internal calibration is carried out by calculating/measuring (experimentally using standard laboratory procedures) each term composing the calibration constant, each representing a source of incertitude relevant parameters of the Lidar system [21]; this method presents larger margins of errors accumulated, and thus is less recommended when accurate measurements are requested, as in the case of humidity profiles to force contrails/cirrus modelling. External calibration efforts often rely on co-located external measurements to ensure accuracy and reliability. Sophisticated techniques use calibration with Integrated Water Vapour IWV quantities [22–24], measured with the independent method, and coaxial configuration could enable Lidar profiling that reaches the ground, while in bi-axial configurations, it would be technically feasible to employ multiple optical receivers simultaneously in such a way that observations can be made close to the surface where the Lidar system is positioned. However, there are still many Lidar configurations with only a single optical receiver.

Bi-axial Lidar WVMR could also be calibrated with respect to a part of the vertically resolved reference profile. In theory, a single point observation of WVMR at an altitude where the overlap functions are sufficiently known and stable is sufficient. It is very complicated to determine the suitable reference for a long-term calibration strategy. References are most commonly provided by radio-sounding [25–30]. This is usually insured by comparing Lidar observations with balloon observations in the lower altitude ranges where balloon sondes exhibit their best accuracy. This method has a serious limitation of discontinuities at individual stations (humidity sensor response, material change, temporal continuity, etc.) and a poor sensitivity in the upper troposphere due to the non-perfect alignment between both profiles caused by the balloon radiosonde derivation from the zenith above the site by wind. Operational on-site radiosondes might be the best option if available and trusted to be insensitive to instrumentals anomalies at severe atmospheric conditions like radiosondes

with a certified GRUAN data products (GRUAN: Global Climate Observing System GCOS Reference Upper-Air Network) [31–33]. Meanwhile, radiosondes do not give a sufficient temporal coverage to calibrate a short term WVMR profile (hourly for example) and detect thereby short-term interesting events on the above site air-mass like contrail formations. These cases need hourly references profiles for calibration.

Many other techniques are capable of providing WVMR referenced profiles for Lidar calibration, like laser diodes, Cryogenic Frost point Hygrometer CFH, balloon-borne frost point hygrometers, or Fourier Transform Infrared Spectroscopy FTIR measurements on meteorological stations [20,22,29,34,35]. These instruments have their potentials as references to describe WVMR in the troposphere, but they have also their limitations. Starting from expensive long-term operational costs and passing by limited accuracy on the upper troposphere.

Satellite-derived water vapour profiles might perform the poorest, yet they could serve as an option in the absence of better information [36].

In the case of IPRAL Lidar, located at SIRTA laboratory (*Site Instrumental de Recherche par Télédétection Atmosphérique*) [37], having bi-axial configuration and single receiver system and where long-term calibration is needed (from 2017 up to now), and fine temporally resolved profiles to describe short atmospheric dynamical events, an alternative reference system as fine resolved modelled data can also be used. The current study discusses a new approach of using the ECMWF most recent reanalysis model (ERA5 hourly data sets [38]) to obtain hourly calibrated IPRAL Raman Lidar WVMR profiles for the very first time and assesses the uncertainties of the produced data set. Section 2 describes the IPRAL Raman wavelengths used to retrieve WVMR, Section 3 cites the different data sources used to calibrate and validate the Lidar measurements, Section 4 details the IPRAL WVMR treatment channel and calibration, Section 5 presents the uncertainties of upper tropospheric calibrated WVMR profiles with respect to nearest radiosondes and ERA5, Section 6 discusses out results, and Section 7 concludes this paper.

2. IPRAL

The IPSL Atmospheric Research Lidar (IPRAL: IPSL Hi-Performance multi-wavelength Raman Lidar for Cloud Aerosol Water Vapour Research) is a multi-wavelengths Lidar deployed 20 km south of Paris at SIRTA [37] laboratory.

IPRAL has six receiving channels, including elastic, and inelastic nitrogen and water vapour channels, and polarisation channels. The configuration and the global system design of IPRAL is schematically described in Figure 1.

The IPRAL Lidar system uses a third harmonic Nd:YAG laser, capable of emitting pulses at 355 nm, which is a common choice for water vapour Lidar systems aiming to reach the upper troposphere altitudes, hence IPRAL combines high Raman scattering efficiency and high-power laser source (375 mJ/pulse). Water vapour and nitrogen Raman scattering shifts the emitted beam wavelength from 355 nm to 407.59 nm and 386.67 nm, respectively [39,40]. The back-scattered light returns are collected by a dual telescope system (T1 and T2): the 20 cm near-range telescope (T2); and the 60 cm far-range telescope (T1) which is used for water vapour (Figure 1). It is then directed into the receiver optics responsible for separating the Raman-shifted signals from other back-scattered light via a series of initial beam splitters: BS4 (Beam Splitter 532/532 nm) which initially separates out the 532 nm elastic signal, allowing only the Raman-shifted light (355 nm and its associated Raman wavelengths) to pass through to the next stages; BS5 (Beam Splitter 1064/532 nm): which further separates out any remaining 1064 nm component, ensuring that only the relevant Raman signals continue; BS6 (Beam Splitter 355/355 nm): finally isolates the 355 nm based Raman signals, directing them toward a series of interference filters (IFF)

that isolate the Raman wavelengths specific to water vapour and nitrogen: IFF3 isolates the water vapour Raman-shifted wavelength at 407.59 nm; IFF6 and IFF7 filter the nitrogen Raman-shifted signal at 386.67 nm. These narrow-band pass optical filters allow only the narrow bands of Raman-shifted light to pass, effectively removing other wavelengths and reducing sky background noise in the signals.

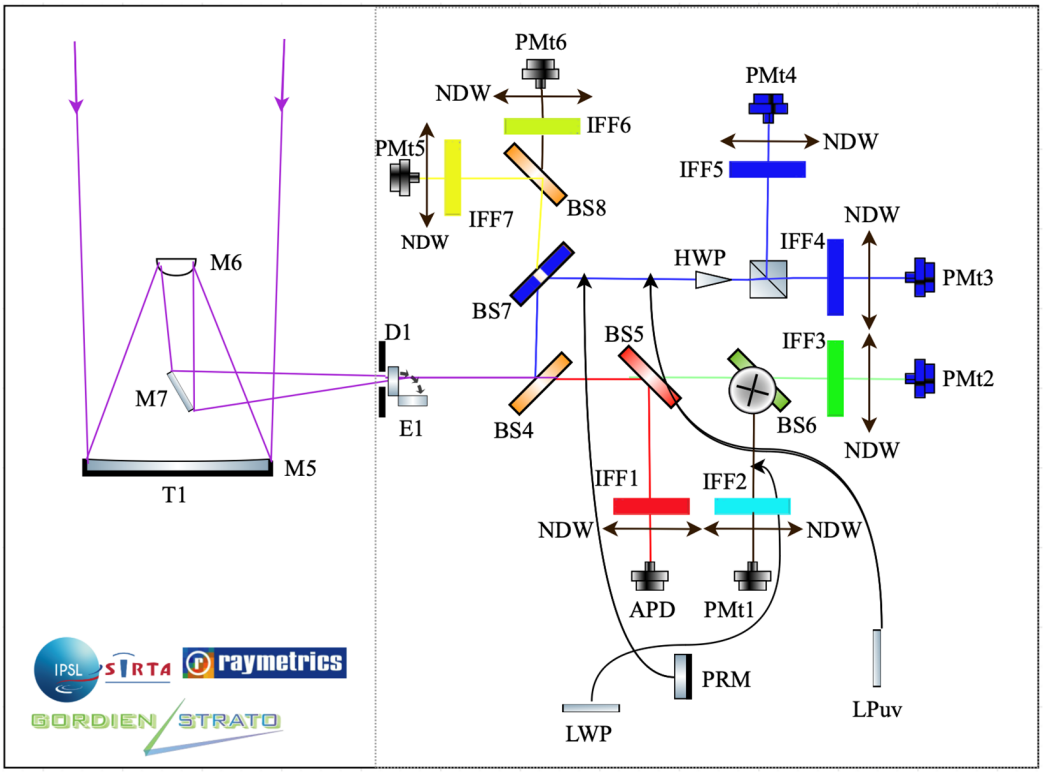

Figure 1. Optical scheme of the IPRAL WVMR Raman concerned parts. We do not present the whole system, but only the optical box components and the corresponding receiver part (starting from the used telescope 'T1', and the neighbour mirrors 'Mi', and passing by the motorised entrance configurations 'D1, E1', towards the beam splitters BSi, and the Photo multipliers PMti, each of which for a certain wavelength). More details about this figure's abbreviations can be found in Table 1.

Table 1. Components of the optical scheme of IPRAL Raman wavelengths presented in Figure 1.

Component	Long Name
Receiver tools	T1: Telescope 60 cm M5: Elliptical Mirror M6: Spherical Mirror M7: Tertiary Plan Mirror
Beam Splitters	BS4: Beam Splitter 532/532 nm BS5: Beam Splitter 1064/1064 nm BS6: Beam Splitter 607/532 nm BS7: Beam Splitter 355/355 nm BS8: Beam Splitter 387/408 nm
Interference Filters	IFF1: Interference Filter 1064.44 nm IFF2: Interference Filter 607.48 nm IFF3: Interference Filter 532.26 nm IFF4: Interference Filter 354.75 nm IFF5: Interference Filter 354.75 nm IFF6: Interference Filter 407.59 nm IFF7: Interference Filter 386.67 nm

Table 1. *Cont.*

Component	Long Name
Photomultipliers	PMt1: Photomultiplier 607 nm PMt5: Photomultiplier 387 nm PMt6: Photomultiplier 408 nm PMt2: Gated Photomultiplier 532 nm PMt3: Gated Photomultiplier 355 nm PMt4: Gated Photomultiplier 355 nm
Divers	NDW: Neutral Density Wheel (6 position, see Figure 1) HWP: Half Wave Plate LPuv: Linear Ultraviolet Polarizer PRM: Partial Reflecting Mirror LWP: Long Wave Pass Optical Edge Filter

The filtered Raman signals then encounter the Neutral Density Wheel (NDW). The NDW contains multiple optical density positions, enabling the control of signal intensity. This component is essential for avoiding Photo-multiplier Tubes (PMt) saturation in high-signal conditions, ensuring stable and consistent signal detection.

After intensity adjustment, the light passes through polarisation components: The Half-Wave Plate (HWP) and Linear Polarizer (LWP) ensure that the polarisation of the Raman-shifted light is aligned appropriately for detection, reducing potential polarisation-related errors; L-PUV is a long-pass optical edge filter that further refines the signal by blocking wavelengths shorter than 593 nm, ensuring the Raman channels receive only the relevant signal components.

The final stage involves Photo-multiplier Tubes (PMts), which detect the isolated Raman-shifted signals: PMT6 detects the water vapour Raman signal at 407.59 nm; PMT2 detects the nitrogen Raman signal at 386.67 nm. These PMts convert the filtered and separated optical signals into electronic signals. The nitrogen Raman signal serves as a reference to normalise the water vapour signal, accounting for variations in atmospheric transmission and laser intensity.

The electronic signals from the PMts are processed and recorded in photon counting mode in function of time (altitude) in order to obtain Raman signals at H_2O and N_2 wavelengths, which is useful for WVMR retrieval.

IPRAL water vapour measurements have not been fully validated. Signal analysis carried out for water vapour measurements and calibration are to be detailed later in Section 4, but let us first discover the used data set for the calibration and the validation.

3. Description of the Used Data Sets

3.1. GRUAN Processed Meteomodem M10 Radiosonde

The nearest meteorological station to the SIRTA laboratory is Trappes (Meteo France station id: 07145), at about 20 km, where regular Meteomodem Co., (located 70 km from Paris, France, at Ury 77760) M10 radiosonde launches are available at midnight and midday.

Being ready for simultaneous water vapour and cloud measurements, IPRAL Lidar has another plus-value performed by the GRUAN [41] regular processing to obtain well calibrated water vapour measurements of the Meteomodem balloon launches. As a step to meet the (GRUAN) requirements [41], few corrections were applied on the M10 radiosondes data set [42]. These corrections concerned the following: (1) the calibration correction; (2) a slow regime due to the slow diffusion of molecules through the sensor, especially at very high and very low relative humidity conditions; (3) the relative humidity sensor dependence on the gradient of temperature; and (4) the time lag at cold temperatures,

which affects measurements in regions of strong relative humidity gradients. GRUAN corrected relative humidity data set [42], being available only since 2018, is used to retrieve the GRUAN WVMR data set, used in the current study, to be compared later (Section 5) with the Lidar calibrated WVMR profiles to assess their uncertainty. GRUAN processed Meteomodem M10 WVMR is retrieved using the corrected relative humidity RH (all corrections applied), the air temperature, and the pressure levels.

3.2. ERA5

ERA5 is a meteorological reanalysis based on a global interactive numerical model and the observations assimilated to optimise the model outputs. The fifth generation of atmospheric reanalysis ECMWF, based on the Integrating Forecasting System (IFS) Cy41r2, which was operational in 2016 is called ERA5 [43]. ERA5 benefits from a decade of developments in model physics, core dynamics and data assimilation to guide and readjust the interactive model's output. For the present study, we use the operational ERA5 product as well as a recent corrected ERA5 variable as detailed in this section.

3.2.1. Operational ERA5 Data Set

ERA5 used data set [38] has a significantly enhanced horizontal resolution of 31 km (0.25°), compared to 80 km for ERA-Interim, and hourly output over 37 pressure levels, and provides a publicly available detailed record of the global atmosphere from 1979 onward. Uncertainty spread of tropospheric humidity samples, mainly random errors, decreases over time. Relative spread is lowest near the surface (5%), but around 15% for specific humidity at 300 h. Pa since 2015 [43].

WVMR is calculated using the specific humidity variable of the nearest pixel to the SIRTA location, with maximal spatial drift of 0.1° and the best temporal coincidence as data are extracted for the same Lidar dominant measurements hours.

ERA5 WVMR profiles are prepared by reversing their altitude arrays to match the ascending altitude sequence of the Lidar instrument; being interpolated onto the Lidar altitude grid.

3.2.2. IAGOS Corrected ERA5

ERA5 Relative humidity variable is calculated on model levels from the 3D specific humidity, temperature, and pressure fields [43]. It is defined as a mixed water/ice relative humidity: with respect to water for temperatures warmer than 0 °C, with respect to ice (RHi) for temperatures colder than −23 °C, and a quadratic interpolation of the two in the 0 °C to −23 °C temperature range.

The European research infrastructure IAGOS [44] (In-Service Aircraft for a Global Observing system IAGOS) provides air composition measurements of several key variables with sensors onboard commercial aircraft. Because of the water vapour variability, it is impossible to have an adequate coincidence between IAGOS flight and IPRAL Lidar, so we aimed to make indirect comparison.

IAGOS humidity measurements [11] served to assess the uncertainty of ERA5 relative humidity at upper troposphere altitudes, and it has been found that ERA5 RHi is about 5–10% drier than IAGOS measurements [9].

Following the same logic, a more recent effort has suggested a corrected ERA5 relative humidity data set based on bi-variate quantile mapping [45]. The corrected data set was recently shared with the scientific community based on the 1995–2022 period IAGOS relative humidity measurements over multi-site; these flights aimed to check operational ERA5 RHi values. Hence, a corrective lookup table was kindly provided by the authors of the study [45] in the framework of the BeCoM project. This table includes corrected RHi values, only for ice supersaturation events where air temperature below 250 k. And

thereby, IAGOS corrected ERA5 midnight hour WVMR data set, for dates coincident to Lidar and GRUAN processed M10 measurements, is generated and is also examined via the comparison to Lidar (Section 5).

4. WVMR Lidar Treatment Channel and Calibration

4.1. WVMR

Atmospheric water vapour concentration is proportional to the ratio of Raman backscattered signals returned at 408 and 387 nm by water vapour and nitrogen, respectively, corrected for sky background noise, accounting for the atmospheric differential transmission T(z) and scaled by the calibration coefficient C (to be detailed later) [46]. Signals are measured by number of photons/bin/shot, and assuming the same overlap functions for both wavelengths. Hence, WVMR is retrieved as the following [46]:

$$\mathrm{WVMR}(z) = \mathrm{C} \cdot T(z) \cdot \frac{S_{H_2O}(z) - B_{H_2O}(z)}{S_{N_2}(z) - B_{N_2}(z)} \quad (1)$$

where

C: The Calibration factor
$T(z)$: The atmospheric differential transmission
$S_{H_2O}(z)$: H_2O Raman signal
$B_{H_2O}(z)$: H_2O Raman Background signal noise
$S_{N_2}(z)$: N_2 Raman signal
$B_{N_2}(z)$: N_2 Raman Background signal noise
$S_{H_2O}(z) - B_{H_2O}(z)$: H_2O Cleaned signal
$S_{N_2}(z) - B_{N_2}(z)$: N_2 Cleaned signal

It has been shown that the relative transmission of both Raman returns in presence of cirrus clouds is negligibly small for altitudes above 4 km. Consequently, no attenuation corrections have been required as soon as the filter rejection are sufficient to eliminate the elastic scattering [39].

4.1.1. Signal Analyses

The IPRAL system operates continuously, but only nocturnal measurements exhibit a signal-to-noise ratio (SNR) sufficient for investigation in the upper troposphere. Nighttime periods are identified using sunrise and sunset times from the Naval Observatory (https://aa.usno.navy.mil/data/RS_OneYear; Accessed on 13 March 2025). To improve the signal-to-noise ratio (SNR), profiles are integrated over successive laser shots per altitude bin, creating a vertical signal profile across fine bins of 15 m for IPRAL. We further enhance the SNR by reducing the vertical resolution by a factor of 10, from 15 m to either 150 m or 300 m, depending on altitude ranges. Previous studies [20,46] recommended a minimum 27 min integration to capture stable air masses and generate a reliable water vapour profile. Here, hourly profiles extending up to 12 km are generated to balance calibration requirements and retain essential information on local variability.

Historical Lidar SNR analyses (2001–2010) over other sites (*Observatoire de haute province* OHP, Saint-Michel-l'Observatoire 04870, France) show that signals above 20 km for the Raman H_2O wavelength and above 50 km for the N_2 wavelength primarily consist of noise. Based on this, the background noise is estimated as the median photon count for altitudes >20 km for water vapour and >50 km for nitrogen signals. The error in this noise estimate is determined through statistical bootstrapping, with 1000 iterations generating re-sampled data sets. The standard deviation of the bootstrapped medians then provides an error estimate for the noise calculation.

We note that water vapour Raman signals are about two orders of magnitude weaker than Nitrogen Raman signals, though the noise magnitude does not follow this same trend (Figure 2). Furthermore, the enhanced signals (resulted after reducing the vertical resolution) extend higher altitudes than raw ones. For example, the IPRAL enhanced water vapour signal can reach up to 12 km, and IPRAL enhanced Nitrogen signal can extend up to about 45 km (Figure 2).

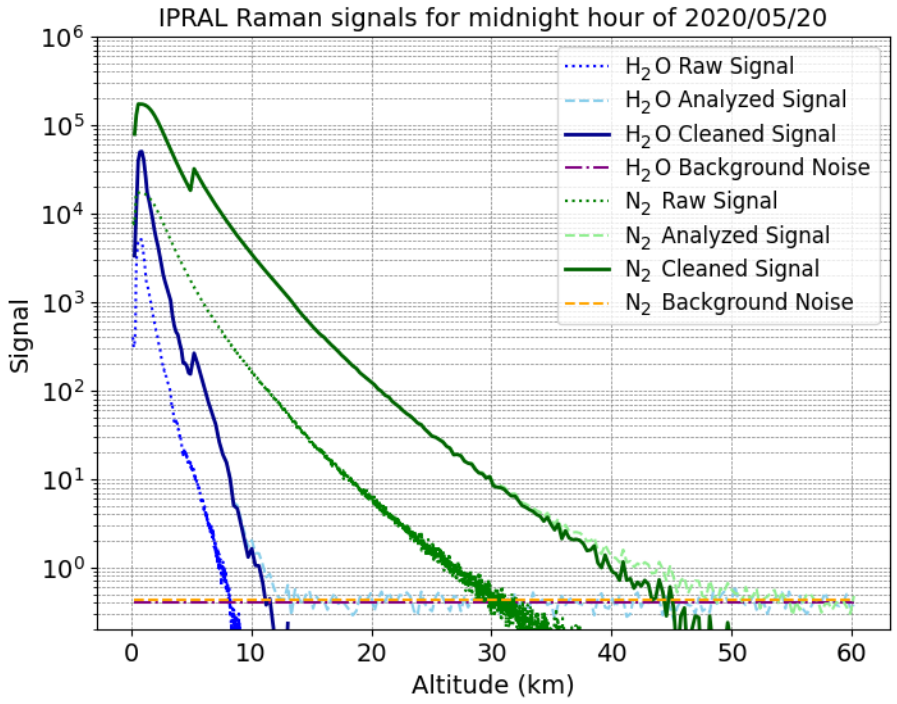

Figure 2. Example of one hour IPRAL Raman lidar signals, (midnight hour of 20 May 2020), water vapour signals are in blue, and nitrogen signals are in green: dotted, dashed, and darker colours are for raw, analysed (with reduced vertical resolution), and cleaned (from sky background noise) Raman signals, respectively. Noise levels are presented in purple and orange for water vapour and nitrogen sky background noise levels, respectively.

4.1.2. WVMR Error Estimation

In theory, the WVMR method is based on a ratio of two simultaneous signals, thus is supposed to be immune to long-term instrumental drift and measurement conditions up to the optical box where both Raman signals are separated. In practice, any change to the Lidar may induce small differential effects. For this reason, some Lidars use hybrid calibration approaches. This was not implemented on IPRAL system; hence, long term calibration would help identifying and quantifying these potential effects, and any drifts in the optical box.

The signal processing related to measurement uncertainties is based on random errors [39]. The two principal error sources considered here are photon counting and skylight background estimation. All equations are provided in Appendix A.

The total WVMR error is calculated for a certain period (hour or even full night), taking into account three sources of uncertainty and variability in the measurements:

a. Calibrated Detection Error: The detection error (Appendix A), representing the uncertainty in detecting and quantifying the WVMR signal, is calibrated to reflect the scaling factors for this hour.
b. Calibrated Noise Error: The noise estimation error (Appendix A) is first calibrated to account for any scaling factors. This calibration process adjusts the noise error for the hour based on the corresponding calibration factor.

c. Calibration Error: This error accounts for any discrepancies or inaccuracies in the calibration procedure, impacting the final WVMR estimation.

The total WVMR error is the sum of the previous three errors.

4.2. WVMR Calibration

While there is no reference for WVMR observation, a statistical approach for calibration is proposed. The experience reveals that ground-based Lidars are quite stable during the night but can be subject to sudden changes when technical changes or settings (or improvements) are performed and require a new calibration coefficient. Lidar water vapour mixing ratio (WVMR) hourly profiles are calibrated using collocated and simultaneous hourly ERA5 reanalysis data [38]. The 37 pressure levels reference is considered, allowing a maximal spatial drift of 0.1° and the best temporal coincident (same Lidar measurements dominant hour).

The calibration process focuses on a specific altitude range, typically between 4 and 6 km above ground level. This range is chosen to ensure that calibration factors are derived from regions of the atmosphere where both Lidar and ERA5 hourly data exhibit reliable measurements [43]. Furthermore, ERA5 shows the best agreement and the least bias to collocated GRUAN processed M10 radiosondes (Root Mean Square Error RMSE does not exceed 0.0002 kg/kg, and significant correlation coefficient better than 80% for all compared profiles). This radiosonde data set [42] is chosen as initial reference to assess the limitations of ERA5 as a calibration reference and thus conclude the best altitude range for calibration. Over 61 compared WVMR midnight hour pairs (ERA5 and GRUAN), and despite large differences observed from one night to another (colourful shades of Figure 3), the median of ERA5 bias does not exceed 5% between 4 and 6 km altitude range of the full WVMR profile (Figure 3).

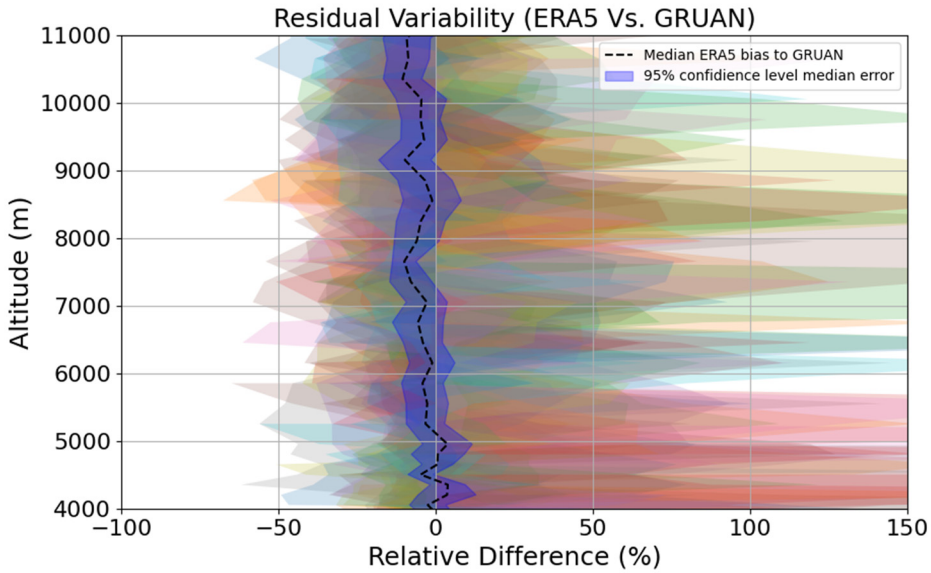

Figure 3. Residual variability of ERA5 to GRUAN processed Meteomodem M10 midnight hours WVMR profiles coincident to IPRAL measurements availability for (2018–2024), median ERA5 bias with respect to GRUAN is shown in dashed black line, surrounded by the pseudo standard deviation error of this bias, which refers to the 95% error confidence level. This comparison is carried out over 61 profiles distinguished by colourful shades to refer to ERA5 relative bias to GRUAN for each profile.

The Lidar calibration procedure starts with hourly screened WVMR profiles, where each altitude bin calibration scale is estimated as the ratio of the Lidar WVMR measure and the (Lidar-like) interpolated ERA5 measure. And so, a point-by-point ratio is calculated, and

the mean of these calibration scales within the selected altitude range (4–6 km) represents an initial calibration factor. This hourly calibration factor represents the scaling factor required to align the Lidar measurement to the ERA5 reference data within the calibration altitude range.

An initial calibrated Lidar profile (between 4 and 6 km retrieved using the initial hourly factor) is compared to ERA5 reference, thereby an initial hourly based calibration error (Root Mean Squared Error (RMSE)) is calculated in order to evaluate the discrepancies between Lidar and ERA5 profiles. Also, correlation coefficient metrics are calculated to assess the accuracy and reliability of the calibration process at the hour scale. Further, only hourly calibration factors issues of significantly correlated profiles (ERA5 and Lidar between 4 and 6 km) are considered. The median of each night-considered hourly factors is named nightly coefficient, and so outlier hours (with a calibration factor out of the 25 to 75% range of this night all hourly factors) are ignored. For example, the hourly calibration coefficients of each night hours during the 2020 year (Figure 4), give nightly calibration factors (median of each night hour factors) ranging between 3 and 7 this year, with a yearly median of around 5.

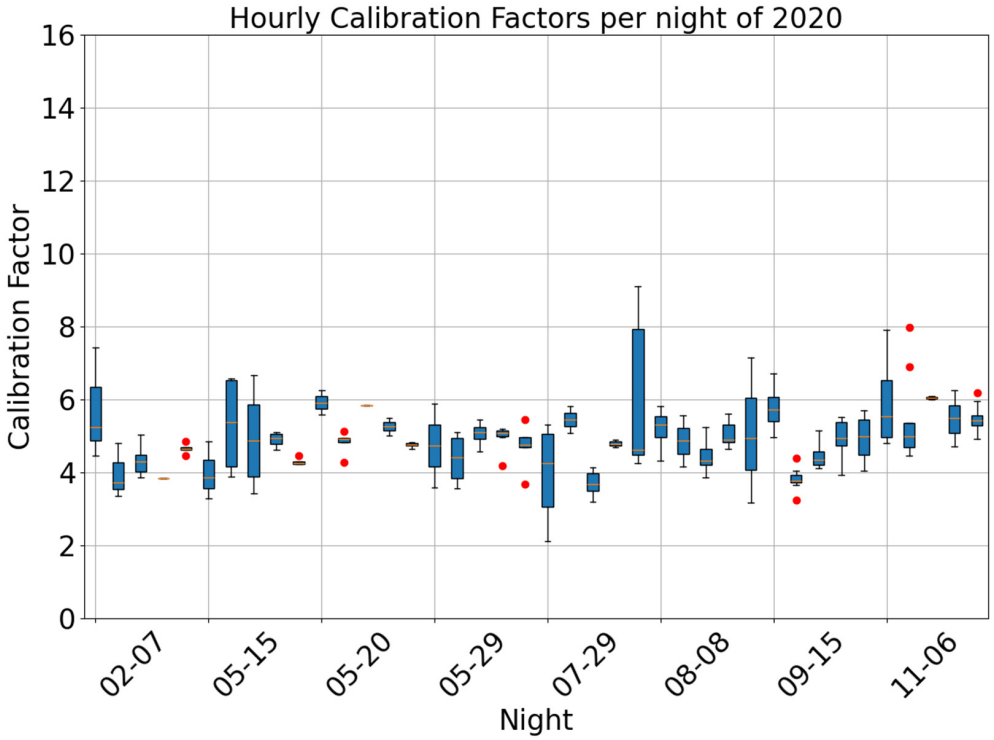

Figure 4. Box-plot of per night hourly calibration factors during 2020. The perbox median is the night calibration factor, and red points are hourly outliers.

The evolution of the nightly calibration coefficients over a long enough period permits one to adjust the series to instrumental changes that are unavoidable in a long commitment (ageing and/or substitution of filters or optical fibres, receiving optic alignment, detectors, etc.) [46]. Moreover, measurements ruptured over more than 2 months are supposed to mark a new later period.

Nightly calibration coefficients (Figure 5a) and the detected instrumental shifts over March 2017–August 2024 period of IPRAL measurements are studied, thus the different stable periods are detected.

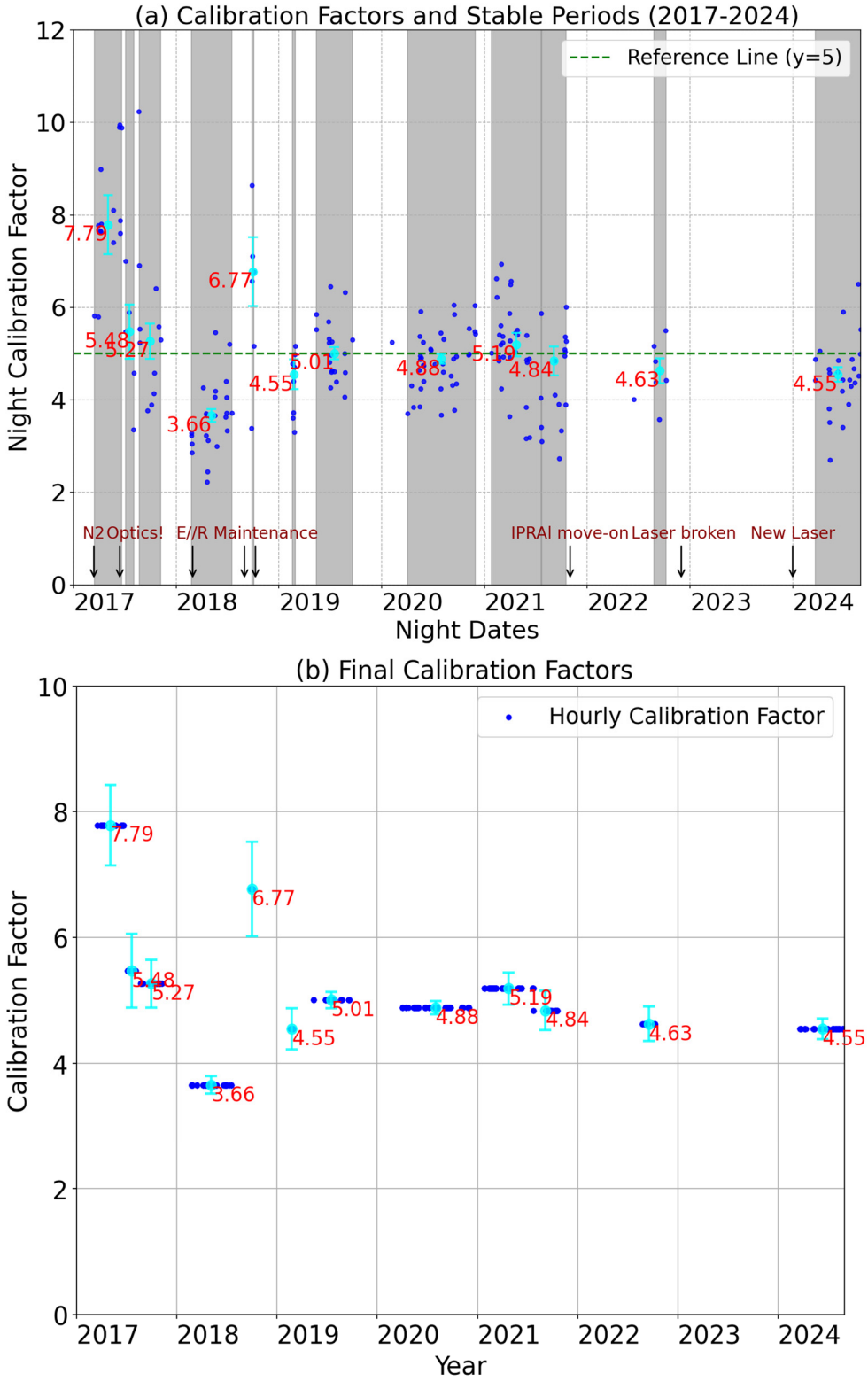

Figure 5. (**a**) Nightly calibration factors of IPRAL WVMR over the 2017 to 2024 period. Grey zones define statistically the periods of instrumental stability, with each period median calibration factor being marked in red values. Blue whiskers is the 95% confidence level error of this factor value. Black arrows refer to the main real events related to IPRAL stability: "N2 Optics" arrows for the drier than reality nitrogen flux problem, "E//R" arrow to refer to the emission/receiver alignment adjustment period. A maintenance period carried out by Lidar expertise is presented by the "Maintenance" arrow. In addition, the "IPRAL move on" arrow refers to the new Lidar room in SIRTA observatory, followed by the laser "break" down event, and the new laser installation in 2024. (**b**) Final WVMR hourly calibration factors to be generalised according to their respective stable periods over 2017–2024, and blue whiskers refer to the respective error at the 95% confidience level.

The IPRAL documentation (technical supports) gives valuable information about the different instrumental anomalies and configuration challenges. However, our calibration process is also able to detect these different phases (marked in red: Figure 5a). We observe (Figure 5a), a first period, marked by the absence of N_2 dry system, and hence the optics were affected by the water condensation problem, which refers to the higher values of the calibration factor for the 2017 year (if compared to later years). This problem was resolved in November 2017 by adding the Nitrogen flux inside the laser head to avoid future water condensation cases. Since April 2018, a better alignment of the emitted laser beam with respect to the telescope field of view (E//R arrow in Figure 5a) is performed. Also, the Second Harmonic Generator SHG and the Third Harmonic Generator THG crystals of the laser were replaced in order to enhance the 355 laser energy, with both previous procedures being marked the first 2018 stable period. The second 2018 stable period followed an intensive maintenance by the Lidar optical designer (Raymetrics Co., Athens, Greece) and the European Lidar expertise (EARLINET) during which the re-adaptation of the NDW position with respect to the 387 channel and the adjustment of the entrance of the optical box to enable lower altitude signals detection without saturation. The latter three periods (since 2019) are marked by less major/unordinary procedures, and so the calibration coefficients have closer magnitudes. IPRAL Lidar was moved to the SIRTA new facility in October 2021, since which the few measurements carried out during 2022 marked also a new stable period. Figure 5a shows a later long measurements discontinuity caused by the laser break-down end of 2022, and purchasing, replacing, and installing a new laser took some time, which explains the long rupture period. Since 2024, a last stable period was marked by the new laser installation.

Further, only Lidar hourly profiles which obtain at least up to 8 km altitude have participated in this calibration. This could justify some discontinuity in the temporal evolution, where the measurement quality control does not enable us to consider these observations. The median of all nightly coefficients between two instrumental changes detected (a stable period) is considered as the «final calibration coefficient» of each measurement performed during this period (Figure 5b). Only after obtaining all hourly final calibration factors (Figure 5b, and as described above), can we retrieve final calibrated WVMR at an hourly scale from raw data.

The hourly WVMR treatment channel steps (Figure 6), are starting from raw Raman signals per very short integration periods (30 s), and very fine vertical resolution (15 m) to be signed to as Level 0, and passing by signal analyses and noise removing, as described in details in Section 4.1.1 in order to obtain cleaned signals (Level 1), without forgetting to calculate signal errors (detection + noise), and retrieving the uncalibrated WVMR, which is a Level 2a product, to be calibrated (using the calibration factor of the same stable period; i.e., the final one generalised over the period at which the measurements belongs), and obtaining finally the hourly calibrated IPRAL WVMR with total WVMR error (Level 2b).

So, the Lidar measurement hour WVMR profile (considered up to altitudes where SNR > 2) is calibrated consistently with a unique calibration factor (generalised over the period of which the measurement date belongs). Analysing some midnight WVMR examples, (ex: Figure 7), we can observe a very good consistency between the IPRAL calibrated WVMR and the nearest GRUAN-processed M10 radiosonde; let us check from a statistical point of view the uncertainties of the newly developed calibrated data set with respect to GRUAN.

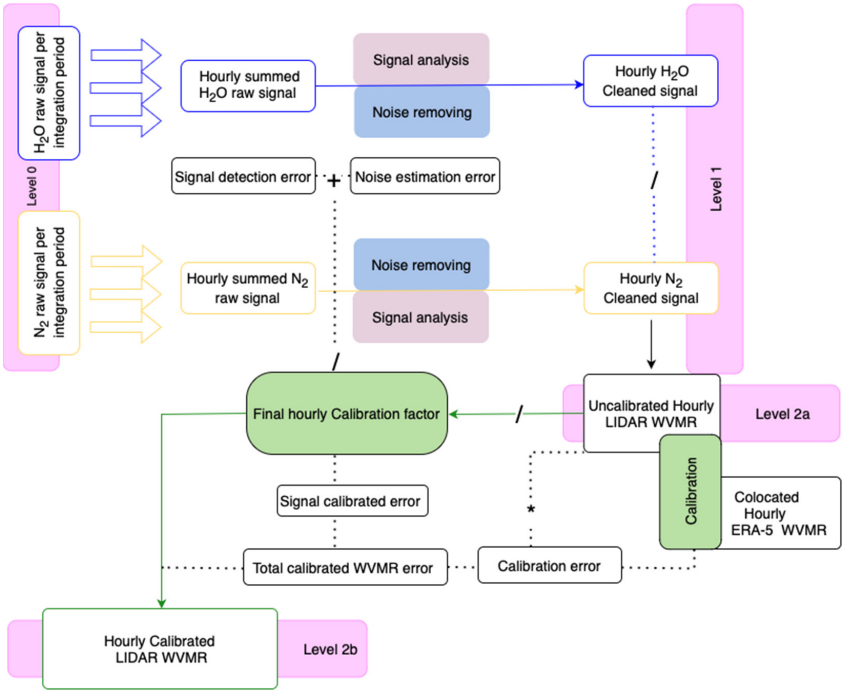

Figure 6. Diagram of Lidar WVMR treatment channel. Starting from Raman signal profiles by integration period and altitude bin (Level 0), passing by summed cleaned signals for one hour (Level 1), and calculating the uncalibrated WVMR profile (Level 2a) as the ratio (/) of both raman signals, to be compared to the ERA5 co-located hourly WVMR between 4 and 6 km, and hence to calculate this hour calibration factor error. Signal calibrated error is obtained from the somme (+) of both signal detection error and noise estimation error considering (by ratio /) the final calibration factor of this hour, the total calibrated WVMR error estimation is detailed in Appendix A. The following symbols: *, /, + is used for multiplication, ratio, and adding items respectively. The final calibrated profile for this hour is retrieved using final factor issue of the period of which belongs the measurement hour.

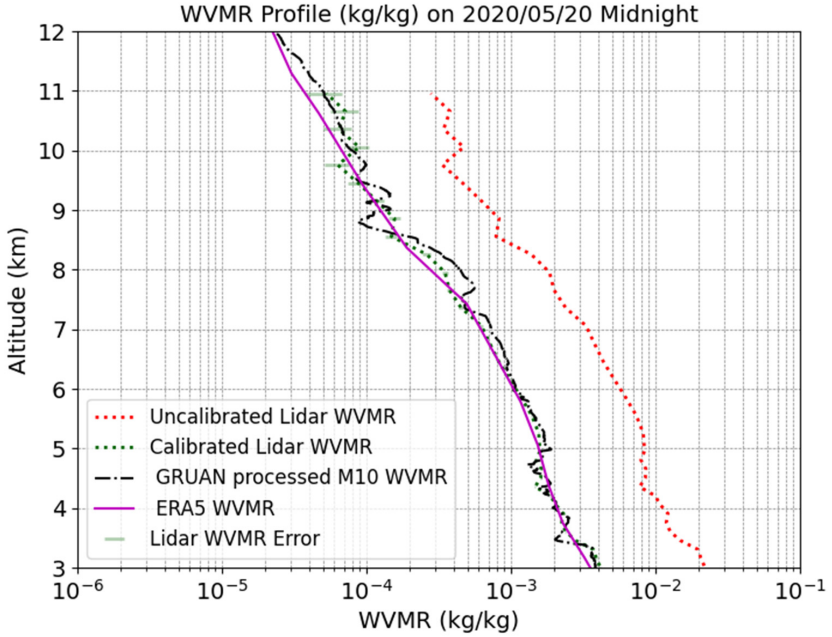

Figure 7. Midnight WVMR profile at 2020/05/20: Uncalibrated Lidar WVMR midnight hour (red pointed line); calibrated Lidar WVMR (green pointed line); total WVMR error is shown with dashed green bars; ERA5 same hour WVMR (purple line); referenced GRUAN processed M10 radiosonde WVMR profile of the midnight launch at the nearest site (Trappes, Meteo France station ID: 07145) is added (dashed black line) to show consistency.

5. Lidar Comparison with Other Datasets

IPRAL WVMR is produced with the objective to assess the Lidar capacities to provide accurate humidity content information at jet-planes altitudes, and hence to obtain very useful information about contrail formation conditions. Hereafter, we present an assessment of the uncertainties of these new Lidar data sets with respect to other well-known sources, including GRUAN corrected radiosondes and ERA5 over altitudes from 7 to 11 km.

5.1. Strategy

IPRAL calibrated WVMR profiles of mid-night hours are compared to available co-located midnight launches. WVMR profiles from GRUAN-processed M10 radiosondes data sets measured at the nearest meteorological station to SIRTA: Trappes [42]. This data set, produced since 2018, allowed the whole comparisons to be carried out over the 2018–2014 period to meet a commune temporal range of all compared data sets.

Since we aim to examine a well-defined altitude range of the WVMR profile, ranged from 7 to 11 km, and since the calibration strategy has been carried out making use of a very different altitude range (4 to 6 km) of the operational ERA5 data set, and since the final generalised factors are inspired by the initial factors but are never the same (Figures 4 and 5a,b), and since the ERA5 humidity profile is retrieved by altitude tranches differently (using adapted formulas), we are also comparing our Lidar WVMR to the midnight hour operational ERA5 profile (Section 3.2.1).

Recent efforts attempt to assess the uncertainty of operational ERA5 relative humidity at cruise altitudes with respect to IAGOS measurement. They suggested a lookup table of ERA5 RHi values [45], as described in Section 3.2.2. We made use of this correction to generate IAGOS-corrected ERA5 midnight hour WVMR data set, with the objective to carry out indirect IAGOS comparison to Lidar and GRUAN coincident dates and thereby validate this correction.

The total number of examined WVMR midnight hour profiles is 61 profiles for each data set, with a commune temporal coverage from 2018 to late August 2024, and one year interruption (2023: year of Lidar laser breakdown).

WVMR profile medians of the whole 61 examined profiles of each data set are well consistent (Figure 8); meanwhile, the other examined datasets seemed to be slightly drier than IPRAL for upper troposphere altitudes (>9 km). One more remark, both ERA5 and IAGOS corrected ERA5 median profiles seemed to be so close, this is partially due to the fact that, what is classified as IAGOS-corrected ERA5 profiles might have only few points/no points corrected within each profile, and so the corrected ERA5 profile is identical to the original ERA5 profile in a case where no ice supersaturation points are there to be corrected. Let us examine the IPRAL WVMR bias with respect to these data sets.

5.2. Lidar vs. RS

The median relative bias (%) of the Lidar WVMR to GRUAN processed M10 radiosondes is analysed over altitudes from 7000 m to 11,000 m. The biases range from −5% to +10%, with variations across different altitude levels (Figure 9). The comparison of co-located profiles shows excellent agreement with significant correlation about ~90% mostly.

Below 8000 m, the relative bias is slightly negative, indicating a more humid GRUAN radiosondes with respect to Lidar WVMR. This small negative bias at lower altitudes might suggest the need for further calibration efforts or retrieval refinement for Lidar. However, it might also be linked to radiosondes' possible shift far away from the zenith of the launch site. Both hypotheses will be further investigated during an upcoming more extensive measurements campaign at SIRTA, mostly in 2025.

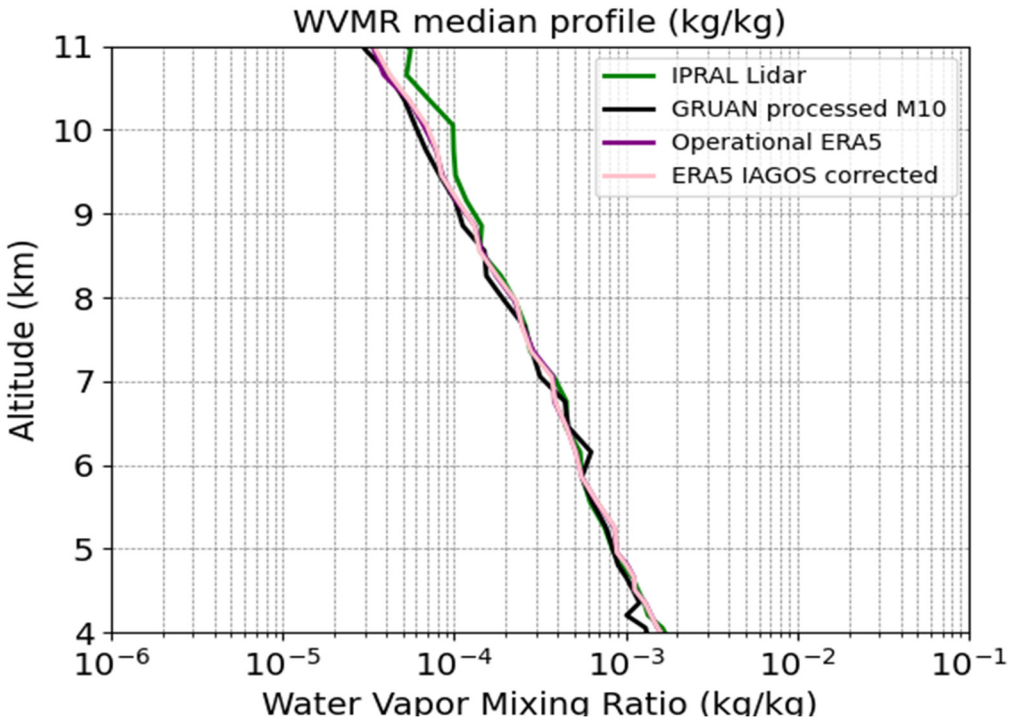

Figure 8. WVMR median profile of the compared data set (median of 61 profiles between 2018 and 2024): Lidar (green), ERA5 (purple), ERA5 IAGOS analysed (pink), and GRUAN processed M10 radiosondes (black).

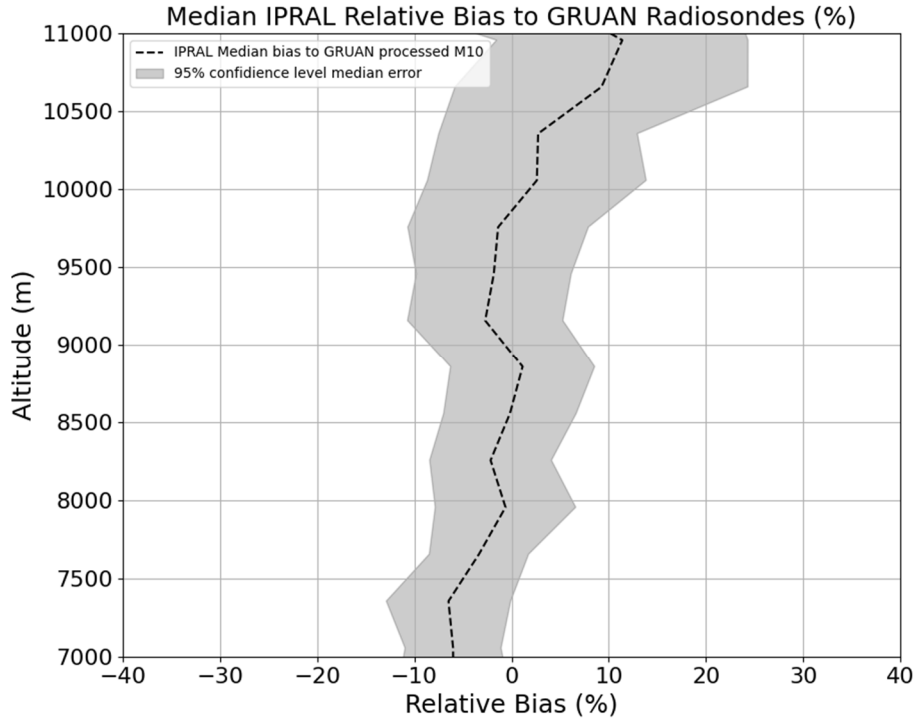

Figure 9. Median IPRAL WVMR relative bias (%) with respect to GRUAN processed M10 radiosondes. Shaded zones refine the 95% confidence level of the relative error.

Upwards, the Lidar and GRUAN profiles have excellent agreement with median bias (around ±5%). This bias is transitioned to positive values for higher altitudes (>10 km), increasing with altitude up to +10%, suggesting a better Lidar sensibility to water vapour content in the upper troposphere, particularly at cruise altitudes (~10–11 km). At these levels, the troposphere often exhibits ice supersaturation events, where traditional radioson-

des may struggle to fully capture the localised humidity variability, which is one evident reason behind the use of GRUAN analysed data set. The larger positive bias above 10,000 m emphasises the Lidar potential utility in capturing atmospheric conditions, particularly related to contrail formation mechanisms at cruise altitudes.

The 95% confidence level of the median value error is assessed by doubling the pseudo standard deviation error (of the relative differences) and normalising it considering the effective number of participated profiles of each altitude bin. This variability becomes more pronounced above 9500 m, where Lidar measurements are often more influenced by reduced signal-to-noise ratios and hence a smaller number of profiles attending 11 km.

The overall good agreement between 8 and 10 km, with biases mostly within ±5%, highlights the Lidar reliable calibration and retrieval performance.

5.3. Lidar vs. ERA5

The median relative bias (%) of IPRAL Lidar WVMR compared to both ERA5 (purple dashed line) and ERA5 corrected with IAGOS (lighter pink dashed line) data sets is displayed in Figure 10. The shaded regions represent variability around the median Lidar bias (at the 95% confidence level). The analysis spans the altitude range of 7000 m to 11,000 m, covering the upper troposphere region. The comparison of collocated profiles confirmed very good agreement with significant correlation (70–90%) mostly. Operational ERA5 data set shows a general dry bias with respect to Lidar.

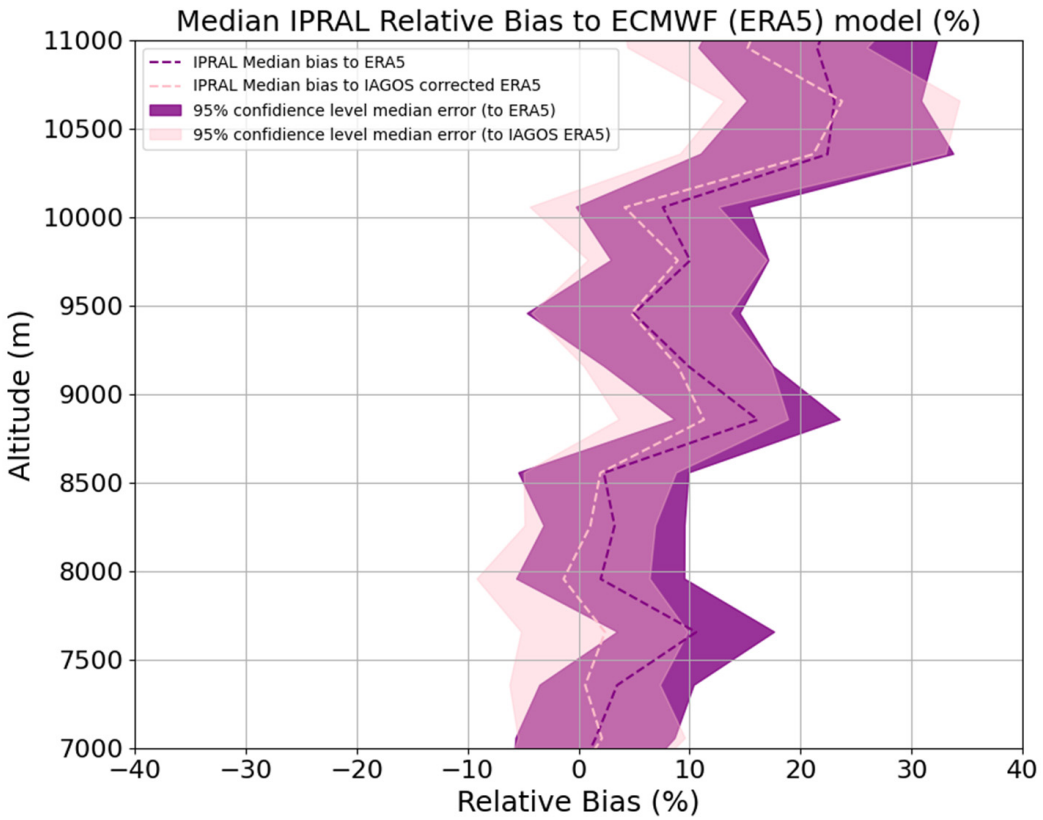

Figure 10. Median IPRAL WVMR relative bias (%) with respect to ERA5 (purple) and IAGOS corrected ERA5 (pink), shaded zones refine the 95% confidence level of the relative error.

Below 8.5 km, both ERA5 data sets (operational/IAGOS-corrected) show relatively small biases with respect to Lidar, around 10% for operational ERA5, whereas the corrected ERA5 data set aligns more closely with the Lidar measurements with nearly no bias (~less than 5%).

ERA5 dry bias increases with altitude, and can reach up to +25% around 11 km. This might suggest that ERA5 underestimates humidity content during ice supersaturation events, as recently cited by [45].

Above 9500 m the biases for both data sets increase slightly, but the IAGOS-corrected ERA5 maintains smaller deviations compared to the uncorrected data set and hence better agreed with Lidar. Our results validate the IAGOS correction, and it shows how this correction permits to compensate the ERA5 dry biases at upper tropospheric altitudes, which could be partially due to the mishandling of ice supersaturation extreme conditions, and hence reduce its bias with respect to Lidar.

The ERA5-IAGOS corrected WVMR data set seemed better agreed with Lidar. However, as the biases are still present within the correction (Figure 10, light pink), our results suggest a systematic ERA5 dry bias on altitudes above 8.5 km. This bias is linked to mishandled conditions other than ice supersaturation events.

6. Discussion

A very first calibration of IPRAL Raman Lidar water vapour mixing ratio (WVMR) profiles is presented by the current research. Its methodology aligns with previous works (e.g., [25,46]) but differ by the external reference used. The reliance on nighttime radiosonde launches, especially GRUAN analysed M10 data sets, in order to evaluate the reference quality in the calibration altitude range with respect to radiosondes, is useful to check how robust the obtained calibration factors are, and also to check the reference quality. GRUAN and ERA5 comparison revealed an excellent agreement at the calibration altitude range (4–6 km), This suggests that ERA5, used as the calibration reference, successfully captures humidity variability in the lower free troposphere.

The SIRTA technical reports of the whole calibrated period provided another independent source to re-evaluate how well the obtained factors account for known instrumental and atmospheric variability. As demonstrated in Section 4, the consistency of these calibration factors across the 2018–2024 period underscores the long-term stability of the Lidar system and the efficacy of the adopted calibration approach. This stability aligns with findings by [47], who emphasised the importance of stable calibration for multi-year assessments of atmospheric water vapour.

In Section 5, the comparison of Lidar WVMR against GRUAN proceeded radiosondes reveals a median relative bias within $\pm$10% for altitudes below 9 km. Lidar WVMR profiles show significant agreement with GRUAN exceeding 90% (significant correlation coefficients). Lidar agreement with GRUAN even gets better with altitude. This underscores the Lidar potential to complement traditional radiosonde measurements for studying atmospheric processes at cruise altitudes, such as those related to contrail formation and aviation-induced climate impacts. This level of agreement is comparable to previous similar inter-comparison studies. For example, refs [20,48] reported biases ranging from 10% to 20% between Lidar WVMR and Cryogenic frost-point hygrometer CFH, RS92 radiosondes, respectively, even if the calibration strategy (and reference) are different. The altitude-dependent radiosondes biases linked to sensor sensitivity in regions of low humidity were highlighted by [42]. Other efforts found comparable results between Raman Lidar WVMR and radiosondes at lower altitudes (<6 km) and [49].

Upper troposphere Lidar WVMR comparison to ERA5 (including the IAGOS corrected data set) shows also general agreement, but an obvious ERA5 dry bias is reported; enhancing with altitude, it seems that ERA5 gives smaller values in the upper troposphere (Figure 11). This might be due to ERA5 insufficient sensibility to detect extreme water vapour content during ice supersaturation events. Such behaviour is probably linked to reduced ERA5 RHi values due to the use of saturation adjustment in the micro-physics

parametrization, or even some form of relaxation method as reported by [7,9,10] for ERA5 and by [50] for ERA-interim.

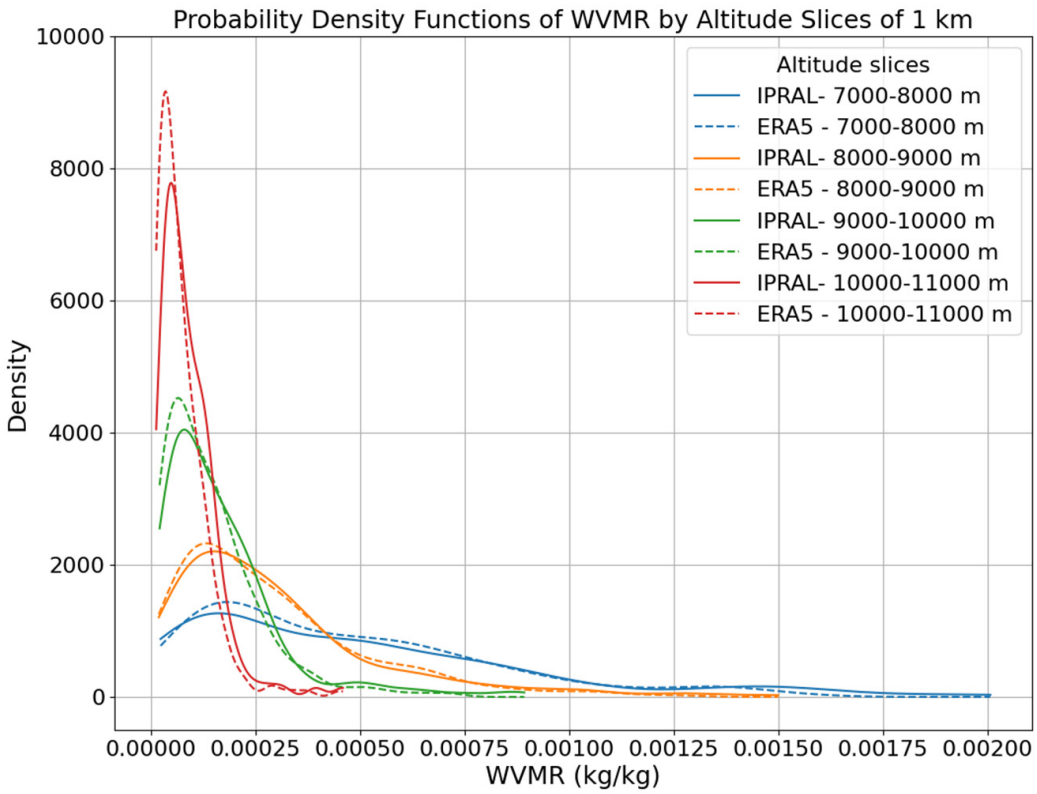

Figure 11. Probability density function of all Lidar WVMR profiles (solid lines) and ERA5 ones (dashed lines) per altitude layer of 1 km (between 7 and 11 km).

IAGOS-corrected ERA5 WVMR data set, adapted using corrected RHi [45], shows significantly better agreement with Lidar, with smaller biases and reduced variability. If we analyse two examples of Lidar WVMR midnight profiles for wet and dry conditions (Figure 12a, Figure 12b, respectively). The wet condition case (Figure 12a) exhibits a slight deviation between the original ERA5 profile and IAGOS corrected ones, by which the latter is becoming closer to the Lidar WVMR profile of the same hour, which exhibits wetter values. While the dry condition case (Figure 12b) did not involve any ERA5 correction based on ice supersaturation conditions, particularly noteworthy is the reduced bias when using the IAGOS-corrected ERA5 data set (Figure 10). This improvement validates the corrections applied to ERA5 by incorporating in situ aircraft measurements, which enhance the model's representation of upper tropospheric humidity. Such findings demonstrated that assimilating high-resolution aircraft data significantly reduces model biases in regions critical for contrail formation and ice supersaturation. However, the remaining persistent ERA5–IAGOS corrected dry bias (Figure 10) with respect to Lidar suggests that there might be other anomalous events affecting ERA5 capacities to detect the right humidity content particularly at upper tropospheric altitudes. Here, we are reporting a possible systematic ERA5 bias linked to other conditions than ice supersaturation events.

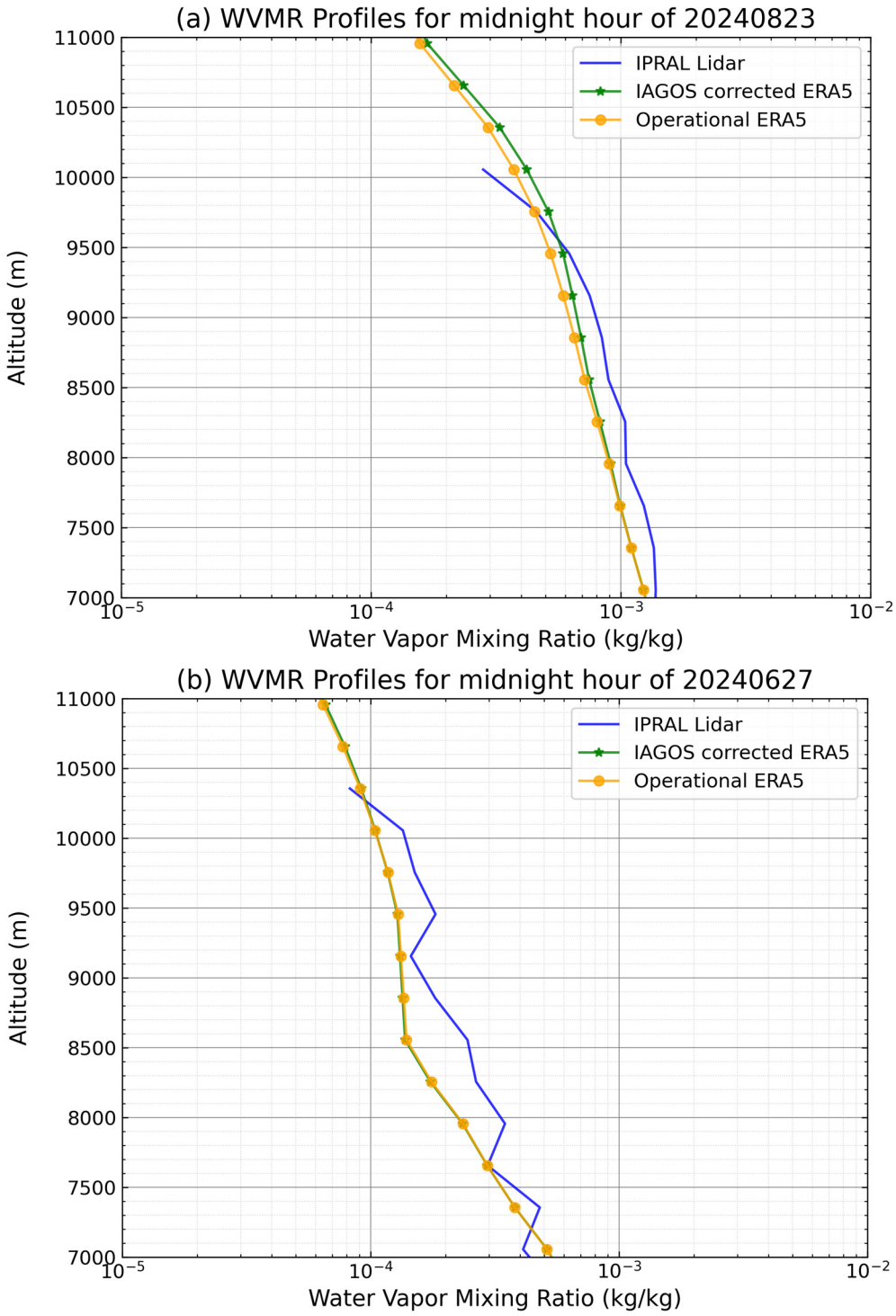

Figure 12. (**a**): Midnight hour WVMR by Lidar (blue), operational ERA5 (orange), and IAGOS corrected ERA5 (green) of 23 August 2024, which is a case of wet water vapour content, and (**b**) idem but of 27 June 2024 where a dry water vapour content was present.

7. Conclusions

Valuable information about humidity content at cruise altitudes over the Parisian region are possibly obtained by IPRAL after calibration. However, their accuracy is subject to careful calibration/validation.

In general, IPRAL derived WVMR shows higher humidity content than the other compared data sets. This may reflect the Lidar sensitivity to detecting low water vapour concentrations. This capability is crucial for studying contrail formation mechanisms and

complements the radiosonde and ERA5 data sets, which often underestimate humidity content at these altitudes.

Overall, the agreement of Lidar WVMR with GRUAN analysed radiosondes and IAGOS corrected ERA5 positions the IPRAL Raman Lidar as a reliable instrument for monitoring water vapour variability, particularly in the upper troposphere.

Key Findings

- **Calibration Reference**: ERA5 was successfully used as the calibration reference, with GRUAN radiosonde data confirming its reliability for this purpose.
- **Consistency with GRUAN**: IPRAL Lidar shows biases of **−5% to +10%** relative to GRUAN analysed radiosondes, improving with altitude.
- **ERA5 Bias**: A **dry bias of 10–20%** in ERA5 relative to IPRAL. This bias might be partially consistent with known underestimations of humidity in ice-supersaturation regions, but it also seemed to be linked to systematic ERA5 bias over upper tropospheric altitudes.
- **Improved ERA5 with IAGOS**: The IAGOS-corrected ERA5 data set reduces biases and variability, validating its corrections and demonstrating the value of in situ data.
- **Lidar Sensitivity**: Raman Lidar's ability to capture humidity variability, especially under supersaturated conditions, complements traditional radiosonde and ERA5 data.

In conclusion, IPRAL Raman Lidar demonstrates excellent agreement with GRUAN analysed radiosondes and improved ERA5 data sets. This supports the growing recognition of Raman Lidar as a valuable tool for numerical weather data assimilation in climate and atmospheric research. Future campaigns will further refine its applications by extending the calibration methodology to tropical Lidar systems and broader atmospheric conditions.

Author Contributions: Conceptualization, P.K.; methodology, D.A. and A.H.; software, J.-C.D., C.P. and F.M.; validation, P.K. and D.A.; formal analysis, D.A.; investigation, D.A., A.H., J.P. and A.S.; resources, P.K.; data curation, D.A. and J.-C.D.; writing—original draft preparation, D.A.; writing—review and editing, F.M., A.F., A.H., C.P. and A.S.; visualisation, D.A.; supervision, P.K.; project administration, P.K.; funding acquisition, P.K. All authors have read and agreed to the published version of the manuscript.

Funding: This project has received funding from the Horizon Europe Research and Innovation Actions program under Grant Agreement N°101056885 through the BeCoM (Better Contrail Mitigation) project and from the French government (BPI) in the frame of France 2030 under Grant DOS0182433/00 for the CONTRAILS project.

Institutional Review Board Statement: Not applicable.

Informed Consent Statement: Not applicable.

Data Availability Statement: ERA5 data set are publicly available at: (https://cds.climate.copernicus.eu/datasets/reanalysis-era5-pressure-levels?tab=download, last access: 22 January 2025), IPRAl level 0 data and GRUAN processed M10 radiosondes data are provided with aide of the SIRTA staff (to obtain permission on IPSL climserv data server).

Acknowledgments: The authors would like to thank the technical and IT staff of IPRAL operations and the whole SIRTA observatory staff as well. Special thanks to Florian Lapouge, Patricia Delville, Marc Antoine Drouin, and Christophe Boitel; the authors would like to thank also Milena Martic (Grodien Strato), Abdanour Irbah (LATMOS) for the valuable discussions.

Conflicts of Interest: Author Antoine Farah was employed by the company Meteomodem Co. Authors Alain Hauchecorne and Jacques Porteneuve were employed by the company Gordien Strato. The remaining authors declare that the research was conducted in the absence of any commercial or financial relationships that could be construed as a potential conflict of interest.

Appendix A

Here, we describe three main sources of Raman Lidar WVMR random errors, (Section 4.1.2):

1. Signal Detection Error

The signal detection error (also referred to as photon-counting error) process is described by Poisson statistics, and the standard deviation of the measurement is $\sigma = \sqrt{N}$, where N is the number of photons counted. This error represents the uncertainty in determining the WVMR due to inherent variations and noise in the Lidar signals. It is estimated based on the cleaned signals of H_2O and N_2, along with the brut signal's respective detection errors. The detection error is calculated as the root mean square (RMS) of the relative errors associated with H_2O and N_2 signals, adjusted by their respective noise levels. This provides a comprehensive assessment of the detection error in the WVMR estimation process as following:

$$\mathrm{WVMR}_{\mathrm{detection}_{\mathrm{err}}} = \sqrt{\left(\frac{1}{\left(S_{N_2}(z) - B_{N_2}(z)\right)} \cdot S_{H_2\mathrm{O,err}}(z)\right)^2 + \left(\frac{S_{H_2O}(z) - B_{H_2O}(z)}{\left(S_{N_2}(z) - B_{N_2}(z)\right)^2} \cdot S_{N_2,\mathrm{err}}(z)\right)^2}$$

where

$S_{N_2}(z)$: N_2 Raman signal
$B_{N_2}(z)$: N_2 Raman Background signal noise
$S_{N_2}(z) - B_{N_2}(z)$: N_2 Cleaned signal
$S_{H_2\mathrm{O,err}}(z)$: H_2O Raman brut signal detection error
$S_{N_2,\mathrm{err}}(z)$: N_2 Raman brut signal detection error
$S_{H_2O}(z) - B_{H_2O}(z)$: H_2O Cleaned signal
Calibrated Detection Error = $\mathrm{WVMR}_{\mathrm{detection}_{\mathrm{err}}} / \mathrm{Calibration}_{\mathrm{factor}}$

2. Noise Detection Error

Similar to the detection error, the noise estimation error is calculated using RMS of the relative errors, reflecting the combined impact of noise estimation inaccuracies on WVMR calculations. the noise estimation error is computed using the following equation:

$$\mathrm{WVMR}_{\mathrm{noise}_{\mathrm{err}}} = \sqrt{\left(\frac{1}{\left(S_{N_2}(z) - B_{N_2}(z)\right)} \cdot B_{H_2\mathrm{O,err}}(z)\right)^2 + \left(\frac{S_{H_2O}(z) - B_{H_2O}(z)}{\left(S_{N_2}(z) - B_{N_2}(z)\right)^2} \cdot B_{N_2,\mathrm{err}}(z)\right)^2}$$

where

$S_{N_2}(z)$: N_2 Raman signal
$B_{N_2}(z)$: N_2 Raman Background signal noise
$S_{N_2}(z) - B_{N_2}(z)$: N_2 Cleaned signal
$B_{H_2\mathrm{O,err}}(z)$: H_2O Background noise estimation error
$B_{N_2,\mathrm{err}}(z)$: N_2 Background noise estimation error
$S_{H_2O}(z) - B_{H_2O}(z)$: H_2O Cleaned signal
Calibrated Noise Error = $\mathrm{WVMR}_{\mathrm{noise}_{\mathrm{err}}} / \mathrm{Calibration}_{\mathrm{factor}}$

3. Calibration Error

This error presents the RMSE between the calibrated Lidar profile and the referenced profile for calibration, taking into account both profiles portions between 4 and 6 km of altitude (calibration zone).

Calibration error = $\mathrm{WVMR}_{\mathrm{Calibration}_{\mathrm{err}}} * \mathrm{WVMR}$

References

1. Gierens, K.; Sausen, R.; Bauder, U.; Eckel, G.; Großmann, K.; Le Clercq, P.; Lee, D.S.; Rauch, B.; Sauer, D.; Voigt, C.; et al. Influence of aviation fuel composition on the formation and lifetime of contrails—A literature review. *CONCAWE Rep.* **2024**, *24*, 1–91.
2. Teoh, R.; Schumann, U.; Gryspeerdt, E.; Shapiro, M.; Molloy, J.; Koudis, G.; Voigt, C.; Stettler, M.E.J. Aviation contrail climate effects in the North Atlantic from 2016 to 2021. *Atmos. Chem. Phys.* **2022**, *22*, 10919–10935. [CrossRef]
3. Bock, L.; Burkhardt, U. Contrail cirrus radiative forcing for future air traffic. *Atmos. Chem. Phys.* **2019**, *19*, 8163–8174. [CrossRef]
4. Singh, D.K.; Sanyal, S.; Wuebbles, D.J. Understanding the role of contrails and contrail cirrus in climate change: A global perspective. *Atmos. Chem. Phys.* **2024**, *24*, 9219–9262. [CrossRef]
5. Irvine, E.A.; Shine, K.P. Ice supersaturation and the potential for contrail formation in a changing climate. *Earth Syst. Dyn.* **2015**, *6*, 555–568. [CrossRef]
6. Wilhelm, L.; Gierens, K.; Rohs, S. Meteorological conditions that promote persistent contrails. *Appl. Sci.* **2022**, *12*, 4450. [CrossRef]
7. Gierens, K.; Matthes, S.; Rohs, S. How well can persistent contrails be predicted? *Aerospace* **2020**, *7*, 169. [CrossRef]
8. Sperber, D.; Gierens, K. Towards a more reliable forecast of ice supersaturation: Concept of a one-moment ice-cloud scheme that avoids saturation adjustment. *Atmos. Chem. Phys.* **2023**, *23*, 15609–15627. [CrossRef]
9. Wolf, K.; Bellouin, N.; Boucher, O.; Rohs, S.; Li, Y. Correction of temperature and relative humidity biases in ERA5 by bivariate quantile mapping: Implications for contrail classification. *EGUsphere* **2023**, *2023*, 1–38.
10. Thompson, G.; Scholzen, C.; O'Donoghue, S.; Haughton, M.; Jones, R.L.; Durant, A.; Farrington, C. On the fidelity of high-resolution numerical weather forecasts of contrail-favorable conditions. *Atmos. Res.* **2024**, *311*, 107663. [CrossRef]
11. Petzold, A.; Neis, P.; Rütimann, M.; Rohs, S.; Berkes, F.; Smit, H.G.J.; Krämer, M.; Spelten, N.; Spichtinger, P.; Nédélec, P.; et al. Ice-supersaturated air masses in the northern mid-latitudes from regular in situ observations by passenger aircraft: Vertical distribution, seasonality and tropospheric fingerprint. *Atmos. Chem. Phys.* **2020**, *20*, 8157–8179. [CrossRef]
12. Winker, D.M.; Pelon, J.R.; McCormick, M.P. CALIPSO mission: Spaceborne lidar for observation of aerosols and clouds. In *Lidar Remote Sensing for Industry and Environment Monitoring III*; SPIE: Bellingham, WA, USA, 2003; pp. 1–11.
13. Dekoutsidis, G.; Groß, S.; Wirth, M.; Krämer, M.; Rolf, C. Characteristics of supersaturation in midlatitude cirrus clouds and their adjacent cloud-free air. *Atmos. Chem. Phys.* **2023**, *23*, 3103–3117.
14. Keckhut, P.; Borchi, F.; Bekki, S.; Hauchecorne, A.; SiLaouina, M. Cirrus classification at midlatitude from systematic lidar observations. *J. Appl. Meteorol. Clim.* **2006**, *45*, 249–258.
15. Groß, S.; Jurkat-Witschas, T.; Li, Q.; Wirth, M.; Urbanek, B.; Krämer, M.; Weigel, R.; Voigt, C. Investigating an indirect aviation effect on mid-latitude cirrus clouds–linking lidar derived optical properties to in-situ measurements. *Atmos. Chem. Phys. Discuss.* **2022**, *23*, 8369–8381.
16. Mandija, F.; Keckhut, P.; Alraddawi, D.; Khaykin, S.; Sarkissian, A. Climatology of Cirrus Clouds over Observatory of Haute-Provence (France) Using Multivariate Analyses on Lidar Profiles. *Atmosphere* **2024**, *15*, 1261. [CrossRef]
17. Hoareau, C.; Keckhut, P.; Baray, J.L.; Robert, L.; Courcoux, Y.; Porteneuve, J.; Vömel, H.; Morel, B. A Raman lidar at La Reunion (20.8 S, 55.5 E) for monitoring water vapour and cirrus distributions in the subtropical upper troposphere: Preliminary analyses and description of a future system. *Atmos. Meas. Tech.* **2012**, *5*, 1333–1348.
18. De Rosa, B.; Di Girolamo, P.; Summa, D. Temperature and water vapour measurements in the framework of the Network for the Detection of Atmospheric Composition Change (NDACC). *Atmos. Meas. Tech.* **2020**, *13*, 405–427. [CrossRef]
19. Leblanc, T.; McDermid, I.S.; Walsh, T.D. Ground-based water vapor Raman lidar measurements up to the upper troposphere and lower stratosphere—Part 2: Data analysis and calibration for long-term monitoring. *Atmos. Meas. Tech. Discuss.* **2011**, *4*, 5111–5145.
20. Dionisi, D.; Keckhut, P.; Courcoux, Y.; Hauchecorne, A.; Porteneuve, J.; Baray, J.L.; de Bellevue, J.L.; Vérèmes, H.; Gabarrot, F.; Payen, G.; et al. Water vapor observations up to the lower stratosphere through the Raman lidar during the Maïdo Lidar Calibration Campaign. *Atmos. Meas. Tech.* **2015**, *8*, 1425–1445. [CrossRef]
21. Venable, D.D.; Whiteman, D.N.; Calhoun, M.N.; Dirisu, A.O.; Connell, R.M.; Landulfo, E. Lamp mapping technique for independent determination of the water vapor mixing ratio calibration factor for a Raman lidar system. *Appl. Opt.* **2011**, *50*, 4622–4632.
22. Leblanc, T.; McDermid, I.S.; Walsh, T.D. Ground-based water vapor Raman lidar measurements up to the upper troposphere and lower stratosphere for long-term monitoring. *Atmos. Meas. Tech.* **2012**, *5*, 17–36. [CrossRef]
23. Dai, G.; Althausen, D.; Hofer, J.; Engelmann, R.; Seifert, P.; Bühl, J.; Mamouri, R.-E.; Wu, S.; Ansmann, A. Calibration of Raman lidar water vapor profiles by means of AERONET photometer observations and GDAS meteorological data. *Atmos. Meas. Tech.* **2018**, *11*, 2735–2748. [CrossRef]
24. Vérèmes, H.; Payen, G.; Keckhut, P.; Duflot, V.; Baray, J.-L.; Cammas, J.-P.; Evan, S.; Posny, F.; Körner, S.; Bosser, P. Validation of the water vapor profiles of the raman lidar at the maïdo observatory (Reunion Island) calibrated with global navigation satellite system integrated water vapor. *Atmosphere* **2019**, *10*, 713. [CrossRef]

25. Whiteman, D.N.; Russo, F.; Demoz, B.; Miloshevich, L.M.; Veselovskii, I.; Hannon, S.; Wang, Z.; Vömel, H.; Schmidlin, F.; Lesht, B.; et al. Analysis of Raman lidar and radiosonde measurements from the AWEX-G field campaign and its relation to Aqua validation. *J. Geophys. Res. Atmos.* **2006**, *111*, D09S09. [CrossRef]
26. Leblanc, T.; McDermid, I.S. Accuracy of Raman lidar water vapor calibration and its applicability to long-term measurements. *Appl. Opt.* **2008**, *47*, 5592–5603. [CrossRef] [PubMed]
27. Adam, M.; Demoz, B.B.; Venable, D.D.; Joseph, E.; Connell, R.; Whiteman, D.N.; Gambacorta, A.; Wei, J.; Shephard, M.W.; Miloshevich, L.M.; et al. Water vapor measurements by Howard University Raman lidar during the WAVES 2006 campaign. *J. Atmos. Ocean. Technol.* **2010**, *27*, 42–60. [CrossRef]
28. Herold, C.; Althausen, D.; Müller, D.; Tesche, M.; Seifert, P.; Engelmann, R.; Flamant, C.; Bhawar, R.; Di Girolamo, P. Comparison of Raman lidar observations of water vapor with COSMO-DE forecasts during COPS 2007. *Weather Forecast.* **2011**, *26*, 1056–1066. [CrossRef]
29. Bock, O.; Bosser, P.; Bourcy, T.; David, L.; Goutail, F.; Hoareau, C.; Keckhut, P.; Legain, D.; Pazmino, A.; Pelon, J.; et al. Accuracy assessment of water vapour measurements from in-situ and remote sensing techniques during the DEMEVAP 2011 campaign at OHP. *Atmos. Meas. Tech. Discuss.* **2013**, *6*, 3439–3509. [CrossRef]
30. Totems, J.; Chazette, P. Calibration of a water vapour Raman lidar with a kite-based humidity sensor. *Atmos. Meas. Tech.* **2016**, *9*, 1083–1094. [CrossRef]
31. Dirksen, R.J.; Bodeker, G.E.; Thorne, P.W.; Merlone, A.; Reale, T.; Wang, J.; Hurst, D.F.; Demoz, B.B.; Gardiner, T.D.; Ingleby, B.; et al. Managing the transition from Vaisala RS92 to RS41 radiosondes within the Global Climate Observing System Reference Upper-Air Network (GRUAN): A progress report. *Geosci. Instrum. Methods Data Syst.* **2020**, *9*, 337–355. [CrossRef]
32. Hicks-Jalali, S.; Sica, R.J.; Haefele, A.; Martucci, G. Calibration of a water vapour Raman lidar using GRUAN-certified radiosondes and a new trajectory method. *Atmos. Meas. Tech.* **2019**, *12*, 3699–3716.
33. Hicks-Jalali, S.; Sica, R.J.; Martucci, G.; Barras, E.M.; Voirin, J.; Haefele, A. A Raman lidar tropospheric water vapour climatology and height-resolved trend analysis over Payerne, Switzerland. *Atmos. Meas. Tech.* **2020**, *20*, 9619–9640.
34. Vömel, H.; David, D.E.; Smith, K. Accuracy of tropospheric and stratospheric water vapor measurements by the cryogenic frost point hygrometer: Instrumental details and observations. *J. Geophys. Res. Atmos.* **2007**, *112*, D08305. [CrossRef]
35. Meyer, J.; Rolf, C.; Schiller, C.; Rohs, S.; Spelten, N.; Afchine, A.; Zöger, M.; Sitnikov, N.; Thornberry, T.D.; Rollins, A.W.; et al. Two decades of water vapor measurements with the FISH fluorescence hygrometer: A review. *Atmos. Chem. Phys.* **2015**, *15*, 8521–8538.
36. Filioglou, M.; Nikandrova, A.; Niemelä, S.; Baars, H.; Mielonen, T.; Leskinen, A.; Brus, D.; Romakkaniemi, S.; Giannakaki, E.; Komppula, M. Profiling water vapor mixing ratios in Finland by means of a Raman lidar, a satellite and a model. *Atmos. Meas. Tech.* **2017**, *10*, 4303–4316.
37. Haeffelin, M.; Barthès, L.; Bock, O.; Boitel, C.; Bony, S.; Bouniol, D.; Chepfer, H.; Chiriaco, M.; Cuesta, J.; Delanoë, J.; et al. SIRTA, a ground-based atmospheric observatory for cloud and aerosol research. In *Annales Geophysicae*; Copernicus GmbH: Göttingen, Germany, 2005; pp. 253–275.
38. Hersbach, H.; Bell, B.; Berrisford, P.; Biavati, G.; Horányi, A.; Muñoz Sabater, J.; Nicolas, J.; Peubey, C.; Radu, R.; Rozum, I.; et al. *ERA5-Hourly Data on Model Levels, ECMWF [Data Set]*; ECMWF: Reading, UK, 2023.
39. Sherlock, V.; Garnier, A.; Hauchecorne, A.; Keckhut, P. Implementation and validation of a Raman lidar measurement of middle and upper tropospheric water vapor. *Appl. Opt.* **1999**, *38*, 5838–5850.
40. Keckhut, P.; Chanin, M.L.; Hauchecorne, A. Stratosphere temperature measurement using Raman lidar. *Appl. Opt.* **1990**, *29*, 5182–5186.
41. Seidel, D.J.; Berger, F.H.; Diamond, H.J.; Dykema, J.; Goodrich, D.; Immler, F.; Murray, W.; Peterson, T.; Sisterson, D.; Sommer, M.; et al. Reference Upper-Air Observations for Climate: Rationale, Progress, and Plans. *Bull. Am. Meteorol. Soc.* **2009**, *90*, 361–369. [CrossRef]
42. Dupont, J.-C.; Haeffelin, M.; Badosa, J.; Clain, G.; Raux, C.; Vignelles, D. Characterization and corrections of relative humidity measurement from Meteomodem M10 radiosondes at midlatitude stations. *J. Atmos. Ocean. Technol.* **2020**, *37*, 857–871.
43. Hersbach, H.; Bell, B.; Berrisford, P.; Hirahara, S.; Horányi, A.; Muñoz-Sabater, J.; Nicolas, J.; Peubey, C.; Radu, R.; Schepers, D.; et al. The ERA5 global reanalysis. *Q. J. R. Meteorol. Soc.* **2020**, *146*, 1999–2049.
44. Petzold, A.; Thouret, V.; Gerbig, C.; Zahn, A.; Brenninkmeijer, C.A.M.; Gallagher, M.; Hermann, M.; Pontaud, M.; Ziereis, H.; Boulanger, D.; et al. Global-scale atmosphere monitoring by in-service aircraft—Current achievements and future prospects of the European Research Infrastructure IAGOS. *Tellus B Chem. Phys. Meteorol.* **2015**, *67*, 28452. [CrossRef]
45. Hofer, S.; Gierens, K.; Rohs, S. How well can persistent contrails be predicted? An update. *Atmos. Chem. Phys.* **2024**, *24*, 7911–7925. [CrossRef]
46. Hoareau, C.; Keckhut, P.; Sarkissian, A.; Baray, J.-L.; Durry, G. Methodology for water monitoring in the upper troposphere with Raman lidar at the Haute-Provence Observatory. *J. Atmos. Ocean. Technol.* **2009**, *26*, 2149–2160.
47. Dinoev, T.; Simeonov, V.; Arshinov, Y.; Bobrovnikov, S.; Ristori, P.; Calpini, B.; Parlange, M.; van den Bergh, H. Raman lidar for meteorological observations, RALMO–Part 1: Instrument description. *Atmos. Meas. Tech.* **2013**, *6*, 1329–1346.

48. Reichardt, J.; Wandinger, U.; Klein, V.; Mattis, I.; Hilber, B. and Begbie, R. RAMSES: German Meteorological Service autonomous Raman lidar for water vapor, temperature, aerosol, and cloud measurements. *Appl. Opt.* **2012**, *51*, 8111–8131.
49. Di Girolamo, P.; De Rosa, B.; Flamant, C.; Summa, D.; Bousquet, O.; Chazette, P.; Totems, J.; Cacciani, M. Water vapor mixing ratio and temperature inter-comparison results in the framework of the Hydrological Cycle in the Mediterranean Experiment—Special Observation Period 1. *Bull. Atmos. Sci. Technol.* **2020**, *1*, 113–153.
50. Reutter, P.; Neis, P.; Rohs, S.; Sauvage, B. Ice supersaturated regions: Properties and validation of ERA-Interim reanalysis with IAGOS in situ water vapour measurements. *Atmos. Chem. Phys.* **2020**, *20*, 787–804.